Alexandrov RESEARCH INSTITUTE OF TECHNOLOGY
N I T I

Phase Diagrams for Multicomponent Systems Containing Corium and Products of its Interaction with NPP Materials

(CORPHAD)

Phase 2

LIQUIDUS TEMPERATURE MEASUREMENTS OF A CORIUM MULTICOMPONENT MIXTURE

Progress report
01/07/03 – 31/11/06

Project title	Phase Diagrams for Multicomponent Systems Containing Corium and Products of its Interaction with NPP Materials (CORPHAD, #1950.2)
Commissioned by	ISTC
File specification	CORPHAD/RCP-0605
Implementing organization	The Alexandrov Research Institute of Technology (NITI) of the Atomic Energy Agency of the Russian Federation 188540, Sosnovy Bor, Leningrad Region, NITI, Russia
Project manager	Name: Yu. N. Aniskevich Signature: Date: November, 2006

Authors

Dr., Prof.	V. B. Khabensky
Dr.	S. V. Bechta
Ph.D.	V. S. Granovsky
Dr., Corr.Mem. RAS	V. V. Gusarov
	V. I. Almyashev
Ph.D.	L. P. Mezentseva
	S. A. Vitol
	E. V. Krushinov
Ph.D.	S. Yu. Kotova
Ph.D.	A.A. Sulatsky
Ph. D.	I. V. Kulagin
Ph. D.	D. B. Lopukh
Ph. D.	A. Yu. Pechenkov
	V. G. Bliznyuk
	V. R. Bulygin
	E. M. Belyaeva
	E. K. Kalyago
	N. E. Kamensky
	R. A. Kosarevsky
	A. V. Lysenko
	A. P. Martynov
	V. V. Martynov
	E. V. Shevchenko

CONTENTS

Introduction

The present work has been carried out within the ISTC CORPHAD Project in order to specify phase diagrams of corium-containing systems for severe accident analysis. This study employed a prototypic multicomponent corium mixture resulting from the interaction of molten core with structural and construction materials of the reactor, concrete shaft and corium catcher. Data on phase transition temperatures are necessary for the optimization of databases used in combination with thermodynamic numerical codes for modeling phase equilibria.

This work, performed at the last stage of the Project, was aimed at experimentally determining T_{liq} of an ex-vessel prototypic multicomponent corium, the composition of which had been proposed by CORPHAD collaborators as follows:

Content, mass %						
UO_2	**SiO_2**	**ZrO_2**	**Al_2O_3**	**CaO**	**FeO**	**Cr_2O_3**
54.2	**13.7**	**17.9**	**1.3**	**3.8**	**7.6**	**1.5**

1. *Facility diagram and experimental technique*

To investigate the silica-containing mixtures, the Rasplav-4 facility has been designed and constructed. Power is supplied by an HF valve generator of the Kristall 401 installation at a frequency of 5.28 MHz. A schematic diagram of the induction furnace with the cold crucible is given in Fig.1.

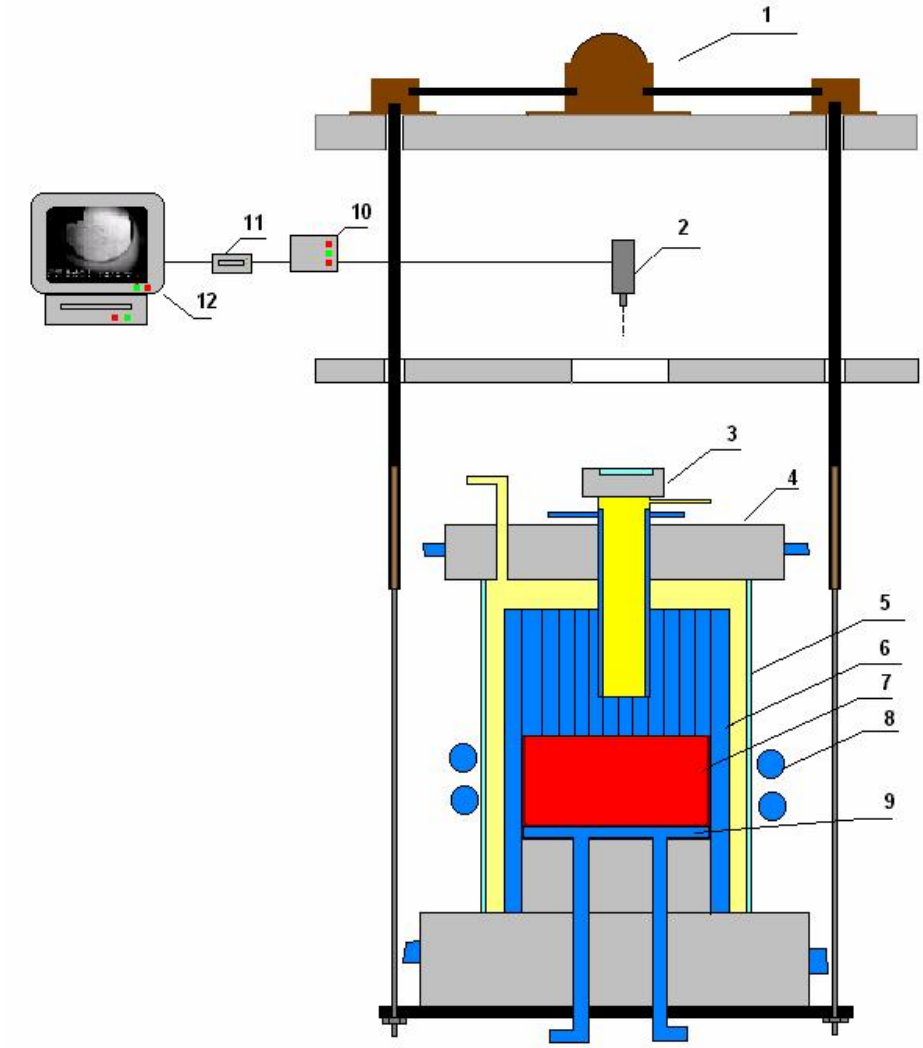

1 – drive for vertical crucible movement 2 – pyrometer coupled with the video camera; 3 – pyrometer shaft; 4– water-cooled lid; 5 – quartz tube; 6 – crucible sections; 7 - melt; 8 - inductor; 9 – bottom calorimeter; 10 – data acquisition system; 11 – device for inserting measurement results into video frames; 12 – monitor/videotape recorder.

Fig. 1. Furnace schematic diagram

Observations of the molten pool surface were carried out using a system of melt surface video registration (11) coupled with the pyrometer (2). This system ensured inserting at 50 Hz of the measured temperature values and the pyrometer sighting spot position into each frame of the video sequence made with the video camera (2) and registered on the videotape recorder (12). The melt surface temperature was measured with the spectral ratio pyrometer RAYTEK MR1-SC. The video camera was registering a melt surface area that was restricted by the shaft diameter to 22 mm. The pyrometer sighting spot was approximately Ø 6mm. The cold crucible internal diameter was 40 mm. The invisible area was an 8 mm-wide ring near the crucible wall.

The melt was sampled in order to determine its composition. T_{liq} was measured by the VPA IMCC method /1/. For this purpose, a free surface of the molten pool, superheated in its bulk, was locally cooled. This was achieved by taking the melt surface out of the inductor and thus decreasing melt temperature only within a very thin surface layer. The surface temperature of the melt coexisting with nuclei of the solid phase (observed in the form of a dark film/crust) was taken as T_{liq}. Then the crucible was brought to the initial position and after the establishment of heat equilibrium and similar conditions of melting, in particular of heat fluxes into the crucible walls and bottom, the procedure was repeated for testing reproducibility of the results.

2. VPA IMCC. CORD46 test

2.1. Charge analysis

When preparing the test, the charge components were checked for the main substance and impurities content.

Silica was introduced into the charge as pressed pellets placed in powdered mixture of other components. Calcium oxide was sintered with zirconia on a zirconia substrate at 1200° C within 4 hours right before adding to the charge with the aim of producing 'calcium zirconate' and removing moisture and carbon dioxide from it.

Aluminium, chromium and silicon oxides were calcinated at 700° C in order to remove moisture (crystal water included) from them.

Composition of the charge is presented in Tab. 1.

Table 1. Charge composition

Components	Main substance content, %	Impurities, mass %	Notes
powdered UO_2, <200 μm dispersivity	>99.0	Fe<0.03; As<0.0003; CuO<0.01; phosphates<0.002; chlorides<0.003.	Passport data, thermogravimetry
powdered ZrO_2, <100 μm dispersivity	(ZrO_2+HfO_2) >99.3	Al_2O_3<0.03; Fe_2O_3<0.05; CaO<0.03; MgO<0.02; SiO_2<0.2; TiO_2<0.1; P_2O_5<0.15; (Na_2O+K_2O)<0.02.	Passport data
FeO	67.68	Fe_2O_3-30.86; Fe-0.57	Chemical analysis results
Fe	>99.9	Si-0.0005; Mg-0.0001; Cu-0.0001; Ni-0.019; Pb-0.0001; Zn-0.00028	Passport data
SiO_2	>98.5	Fe-0.001, Pb-0.002, nitrates-0.001, sulphates-0.01, chlorides–0.001	
CaO	>96.0	Total nitrogen-0.06, carbonate-2.5, sulphates-0.05, chlorides-0.015, Fe-0.02	
Al_2O_3	>97.0	Si<0.05, chlorides<0.05, sulphates <0.2, Fe<0.05, alkaline metals <0.1	
Cr_2O_3	>99.0	Chlorides <0.003, sulphates <0.01, Fe<0.01, water-soluble substances-0.1, Pb-0.005	

In order to perform the test, the crucible was loaded with the specified components (Tab. 2). It should be noted that the charge components were uniformly distributed along the height.

Table 2. Crucible charge composition

Content, mass%							Charge mass, g
UO_2	SiO_2	ZrO_2	Al_2O_3	CaO	FeO	Cr_2O_3	
54.2	13.7	17.9	1.3	3.8	7.6	1.5	300

2.2. CORD46 experimental procedure

The use of IMCC method for preparing a melt containing silicon and calcium oxides is problematic due to low electric conductivity of melts and a high rate of evaporation. To achieve iron oxide stoichiometry in the form of wustite, nitrogen was chosen as an inert atmosphere.

At the initial stage of the test, the startup heating was provided and the molten pool produced. During the charge melting and shrinking, crusts composed of sintered charge formed on the crucible sections above the molten pool surface and could not be knocked down into the melt. The pool depth and bottom crust thickness measured with a probe were 35 and 15 mm, respectively. The pool surface temperature was about 2400° C (Fig. 2), and intensive aerosol formation was observed. An increase of power in the melt did not lead to dissolution of the bottom crust. Thus, composition of the produced molten pool may differ from the average charge composition because of the nonmelted crusts and the bottom crust. After exposure and homogenization of the molten pool, T_{liq} measurements and melt rod sampling were repeated 3 times. Two measurements, i.e. the 2nd and 3rd ones, were a success, and T_{liq} was found to be 2219 and 2221±30˚ C (Fig. 3), with an average of 2220±30˚C. After measurements heating was switched off and the ingot was crystallized in nitrogen.

Fig. 2 shows the history of anode voltage, HF generator current, melt surface temperature, as well as the time of melt sampling.

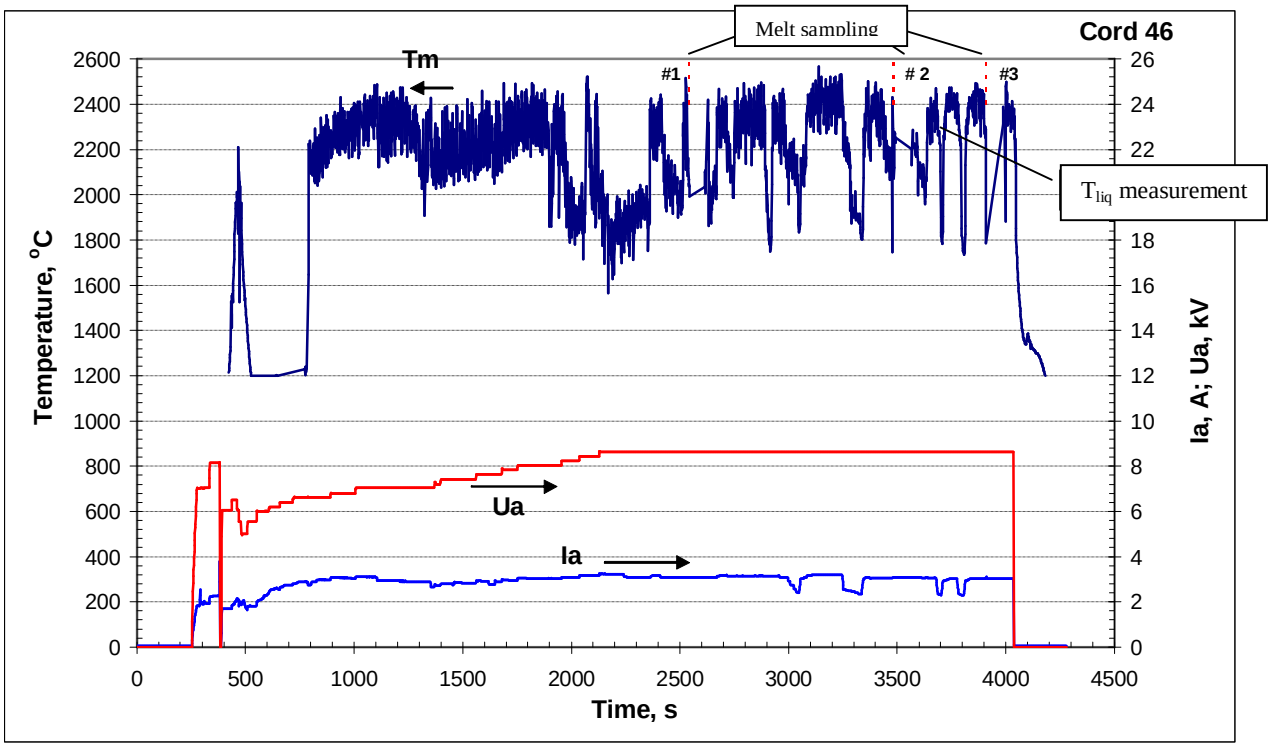

Fig.2. History of melt surface temperature (Tm), anode current (Ia) and anode voltage (Ua)

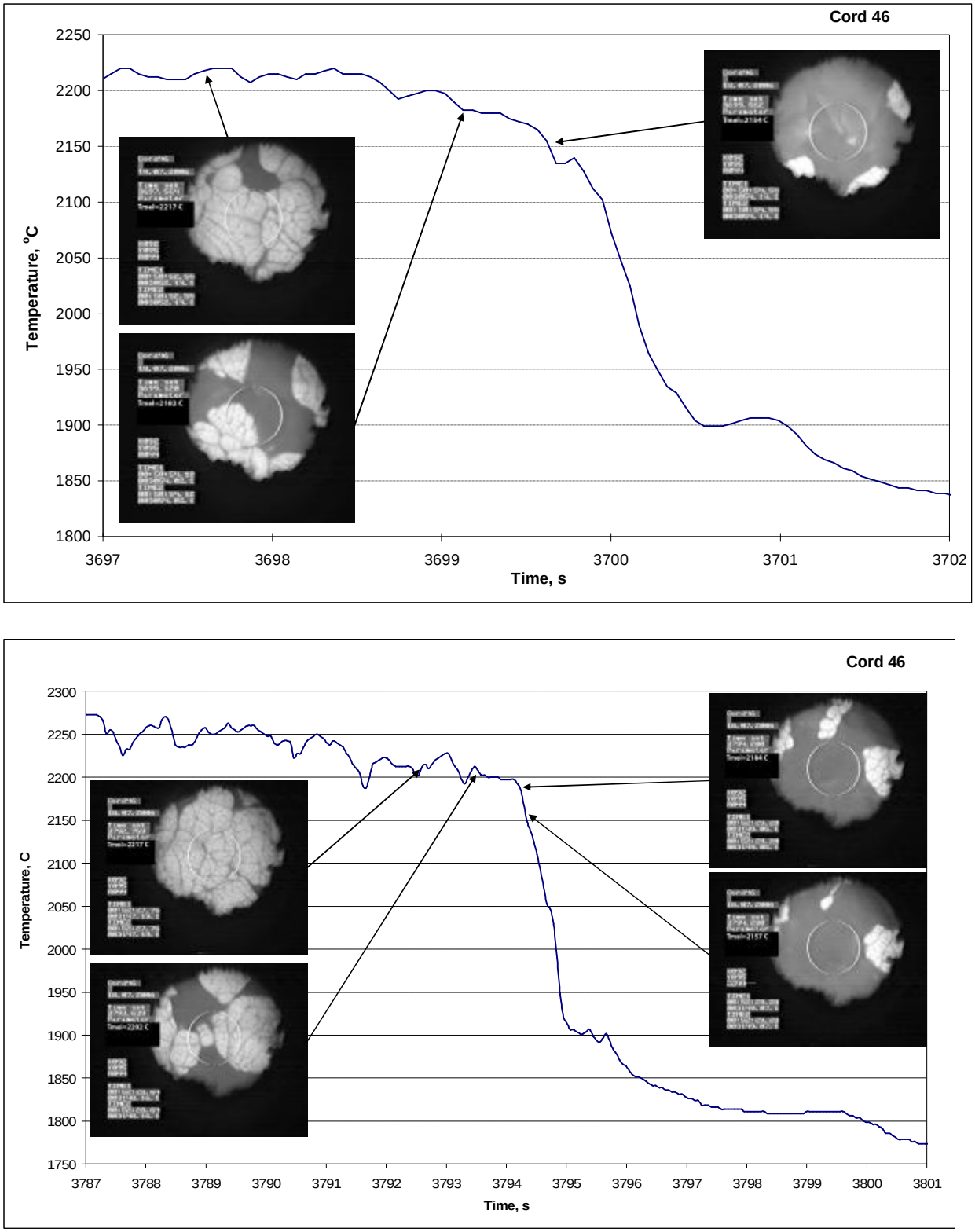

Fig. 3. Fragments of thermograms from CORD46 with inserted melt surface images

3. Posttest analysis

3.1. Material balance

After the test, all materials were taken from the crucible and weighed with a 0.1 g accuracy. The extracted ingot was embedded in epoxy and cat along the axis in for preparing a template for SEM/EDX. Melt samples, crust and spillages were used for preparing samples for XRF in order to determine composition of the melt, for which T_{liq} had been measured. Material balance for the test is given in Tab. 3.

Table 3. Material balance

Introduced into the crucible, g		Collected, g	
ZrO_2	45.6	**Ingot**	195.7
Zr	6.0	**Rod sample 1**	2.9
UO_2	162.6	**Rod sample 2**	2.4
SiO_2	41.9	**Rod sample 3**	3.5
CaO	11.9	**Probe sample**	2.4
Al_2O_3	3.9	**Aerosols**	9.2
FeO	20.6	**Nonmelted charge**	30.0
Fe	2.3	**Above-melt crust**	52.8
Cr_2O_3	4.5		
Σ	**299.3**	**Σ**	**298.9**
Debalance	**0.4**		

Metallic zirconium was used as the startup material, while metallic iron was used for achieving FeO stoichiometry. It is apparent from the given balance that 30% of the initially loaded material is missing in the ingot and it is important to determine true composition of the melt.

3.2. X-ray fluorescence

The elemental composition of the fused products was determined by XRF using the SPECTROSCAN MAX-GV spectrometer /2/.

For this analysis, a technique of compacted pellets was applied to the preparations. All the works on samples preparation for the analysis were performed in argon. At first, the samples were crushed down to grains sized no more than 2 mm. Then an average sample was taken by quartering and milled into particles sized no more than 50 μm. All the obtained results are summarized in Tab. 4.

Table 4. XRF results

Sample	Content, mass%						
	UO_2	ZrO_2	FeO	SiO_2	CaO	Al_2O_3	Cr_2O_3
Rod sample 1	54.9	19.3	7.9	12.5	3.5	0.1	1.8
Rod sample 2	53.9	18.7	7.6	13.4	3.8	0.7	1.9
Rod sample 3	53.0	18.6	7.8	12.9	3.8	2.0	1.9
Above-melt crust	49.9	21.3	5.8	15.6	4.4	1.4	1.6
Nonmelted charge	44.5	21.1	11.6	3.2	4.4	11.6	3.6

The analysis of melt samples taken during the test showed just a slight deviation from the specified composition despite the considerable mass of the nonmelted part of the initially loaded charge. We believe, this may be due to its homogeneity.

3.3. SEM/EDX analysis

Microstructure and elemental composition of the samples were studied by means of scanning electron microscopy (SEM) and energy dispersive X-ray spectrometry (EDX).

The study employed the ABT-55 scanning electron microscope, and the OxfordLink microprobe attachment was used for the elemental analysis of the samples' regions marked for examination.

The spectral characteristic was taken for each sample for determining its integral composition and that for each separate phase. The quantitative analysis was made by comparing spectral intensity of the reference (superpure, specially prepared substances) and studied samples. The used references of U, Zr, Cr, Fe, Si, Ca, Ni were a part of the Link microprobe attachment set.

The threshold of reliable element identification depends on its sequential number in the Mendeleyev's periodic table and varies from 0.3 to 0.5 mass %. Detection of smaller quantities of elements is unreliable.

The EDX analyzer of the ABT-55 microscope is insensitive to light elements (to oxygen, for instance), therefore the quantity of oxygen was determined with this instrument from the mass deficiency and the error was ~5 mass %.

Templates were made from the melt samples taken during T_{liq} measurements. The results of their analysis are given in Figs. 4-6 and in Tabs. 5-7.

Microstructurally, all samples are fine-crystalline, dendritic, and it indicates quenching conditions of crystallization.

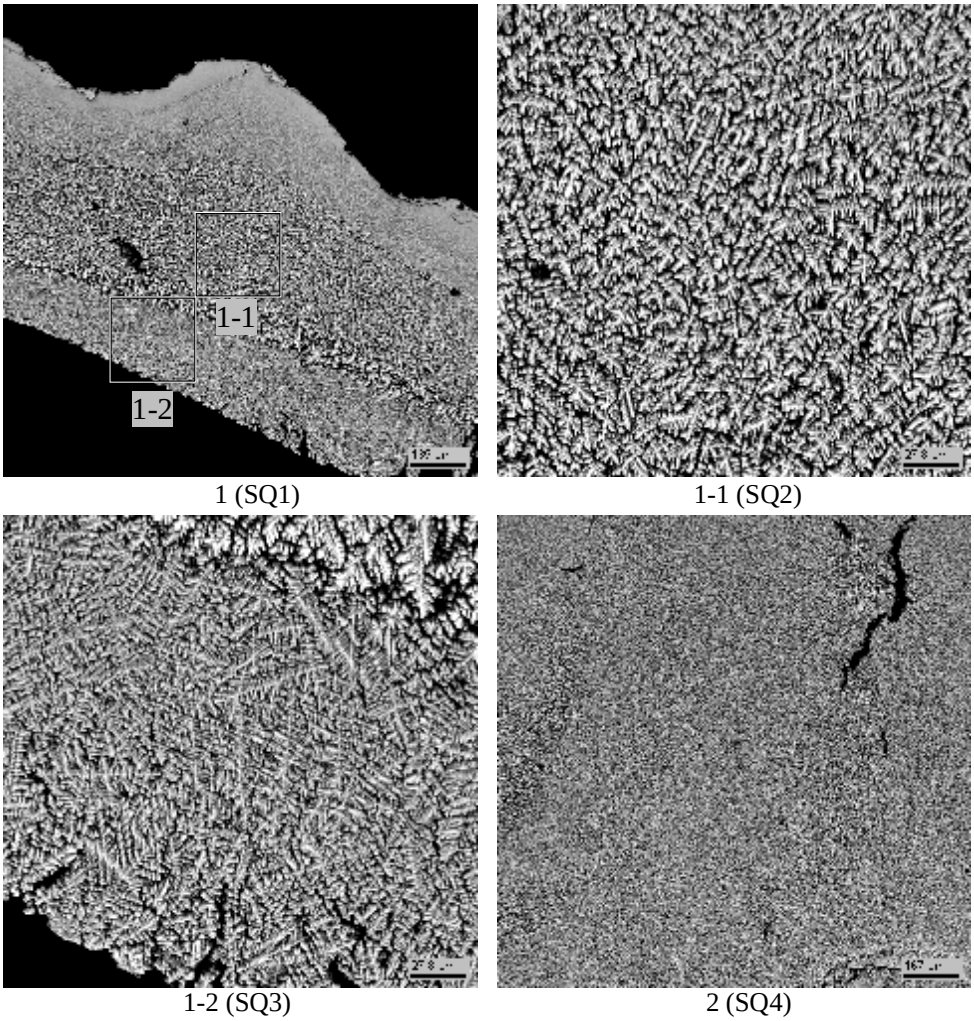

1 (SQ1) 1-1 (SQ2)

1-2 (SQ3) 2 (SQ4)

Fig. 4. Micrographs of rod sample 1

Table 5. EDX data for sample 1

No.		UO_2	ZrO_2	SiO_2	CaO	$AlO_{1.5}$	FeO	$CrO_{1.5}$
SQ1	mass%	53.19	11.82	16.55	4.78	2.08	9.22	2.36
	mol.%	23.07	11.24	32.26	9.98	4.78	15.02	3.64
SQ2	mass%	51.70	11.86	17.56	5.16	2.22	9.47	2.04
	mol.%	21.91	11.01	33.43	10.52	4.98	15.08	3.07
SQ3	mass%	53.00	11.81	16.72	4.96	2.27	9.21	2.04
	mol.%	22.87	11.16	32.43	10.31	5.18	14.93	3.12
SQ4	mass%	51.67	12.11	17.24	5.18	2.26	9.25	2.30
	mol.%	21.94	11.26	32.89	10.59	5.09	14.76	3.47

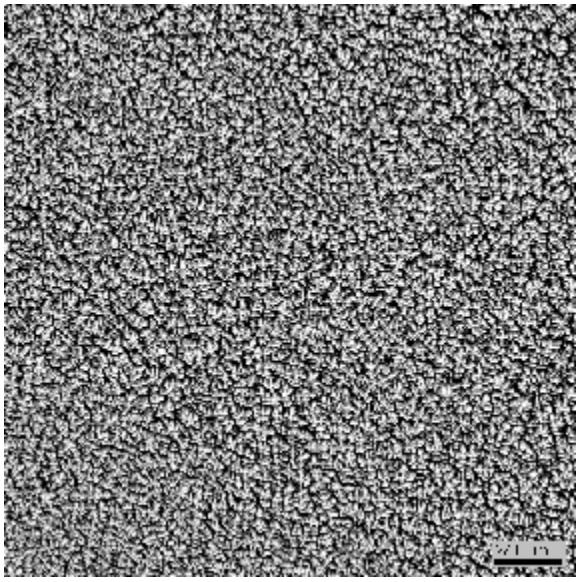

1 (SQ1)

Fig. 5. Micrographs of rod sample 2

Table 6. EDX data for sample 2

No.		UO_2	ZrO_2	SiO_2	CaO	$AlO_{1.5}$	FeO	$CrO_{1.5}$
SQ1	mass%	53.73	12.12	15.86	5.13	1.84	9.28	2.04
	mol.%	23.55	11.64	31.25	10.82	4.26	15.29	3.18

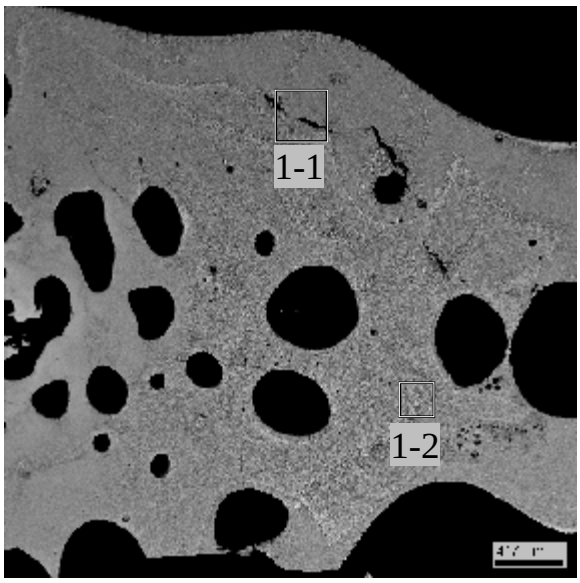

1 (SQ1)

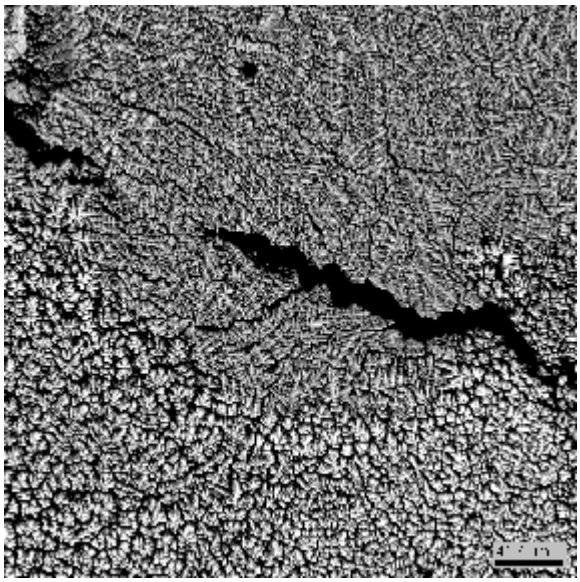

1-1

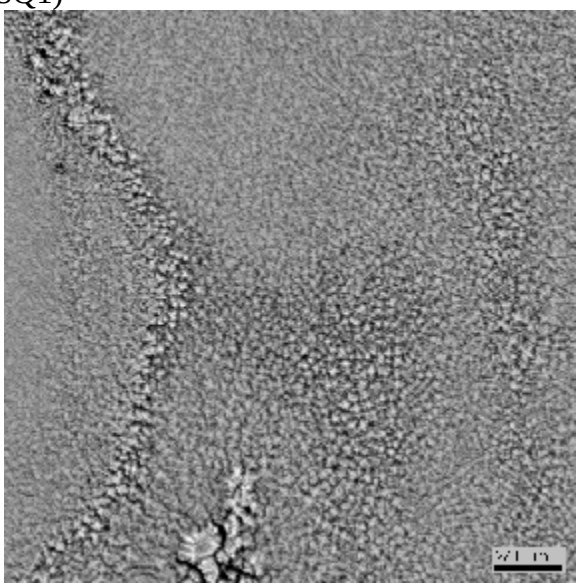

1-2 (SQ2)

Fig. 6. Micrographs of rod sample 3

Table 7. EDX data for sample 3

No.		UO_2	ZrO_2	SiO_2	CaO	$AlO_{1.5}$	FeO	$CrO_{1.5}$
SQ1	mass%	53.06	11.44	16.60	5.06	2.04	9.70	2.10
	mol.%	22.89	10.81	32.18	10.51	4.66	15.72	3.23
SQ2	mass%	54.26	12.24	15.18	5.17	1.75	9.45	1.96
	mol.%	24.02	11.88	30.20	11.02	4.10	15.71	3.08

Composition of the analyzed regions of the samples virtually coincides and denotes homogenic composition of the molten pool during T_{liq} measurements. Notable is that the melt became poorer in ZrO_2 and richer in SiO_2. This may be due to crystallization of the refractory phase along the cold crucible periphery, or to the loss of material in crusts and spillages.

After melt sampling, the bulk melt was quenched and the resulting ingot was later subjected to SEM/EDX analysis.

The diagram of studying the ingot longitudinal section is given in Fig. 7, and the results of SEM/EDX analysis are presented in Figs. 8-11 and in Tabs. 8-11.

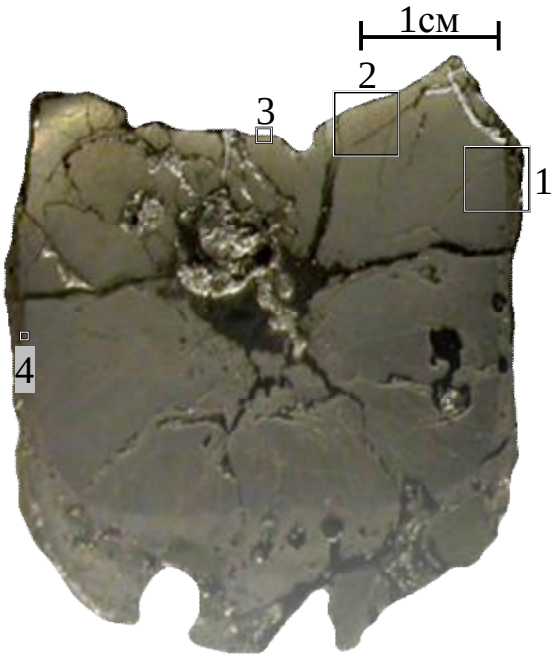

Fig. 7. Longitudinal section of the ingot from CORD46 with regions marked for SEM/EDX analysis

Fig. 8 presents the upper peripheral zone of the ingot (region 1).

The results given in Tab. 8 show that the ingot edges represent the crystallized refractory phase composed predominantly of UO_2 (SQ1, P1).

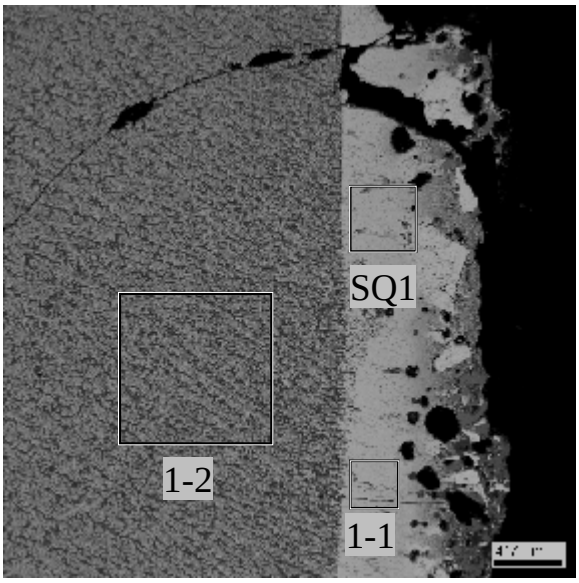

1

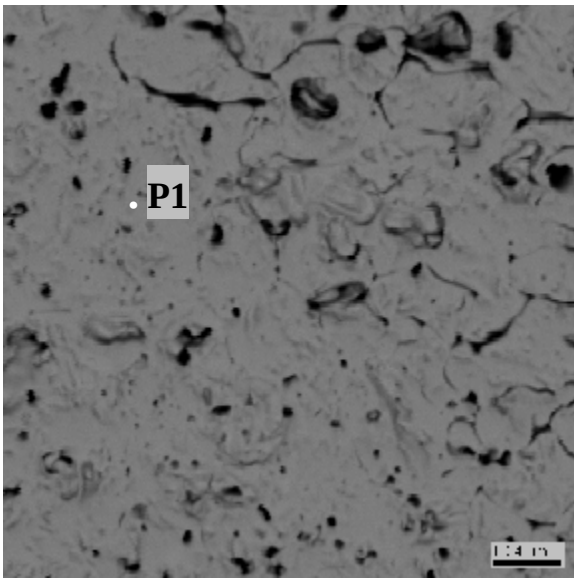

1-1 (SQ2)

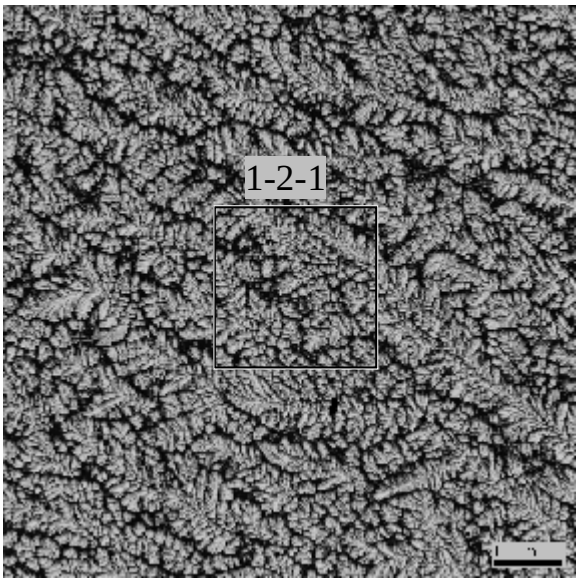

1-2 (SQ3)

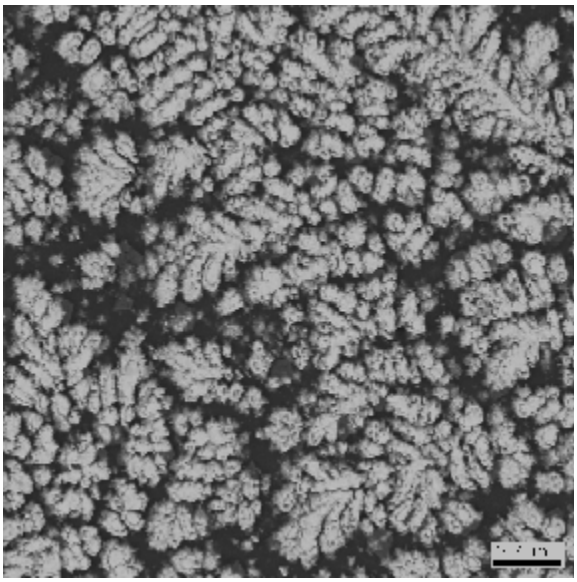

1-2-1 (SQ4)

Fig. 8. Micrographs of region 1

Table 8. EDX data for region 1

No.		UO_2	ZrO_2	SiO_2	CaO	$AlO_{1.5}$	FeO	$CrO_{1.5}$
SQ1	mass%	95.22	1.28	0.93	0.77	1.13	0.68	-
	mol.%	83.22	2.45	3.65	3.22	5.22	2.23	-
SQ2	mass%	95.97	0.70	0.85	0.79	1.06	0.63	-
	mol.%	84.84	1.35	3.37	3.38	4.94	2.11	-
SQ3	mass%	47.41	11.96	18.96	6.04	2.29	10.80	2.54
	mol.%	18.99	10.49	34.13	11.66	4.87	16.25	3.61
SQ4	mass%	46.16	11.92	19.55	6.24	2.40	11.31	2.41
	mol.%	18.17	10.28	34.59	11.83	5.01	16.73	3.37
P1	mass%	98.84	-	0.44	-	0.72	-	-
	mol.%	94.45	-	1.91	-	3.64	-	-

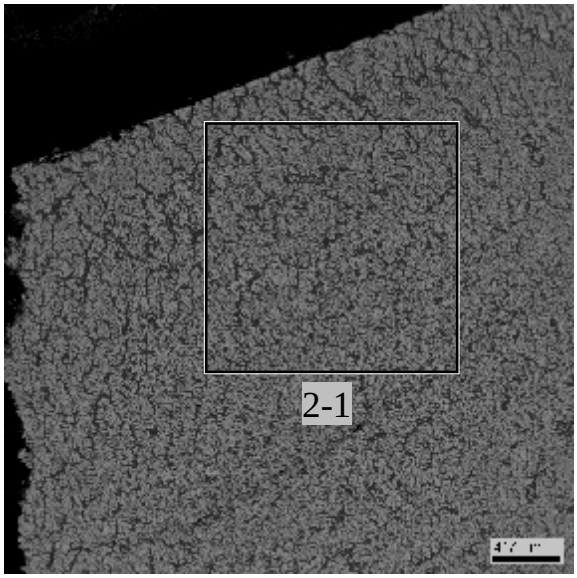

2

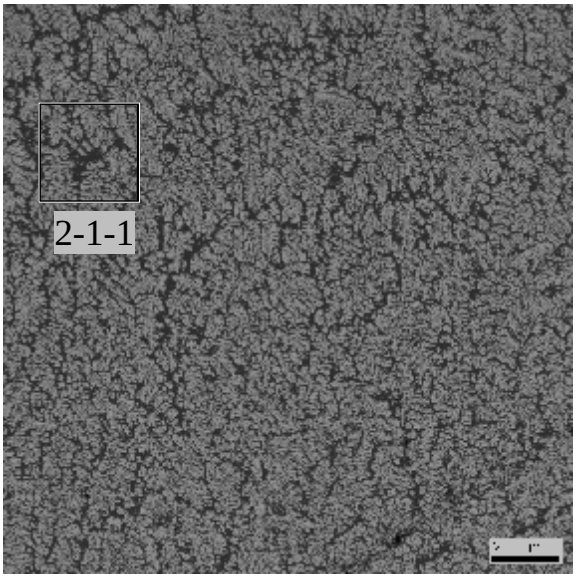

2-1 (SQ1)

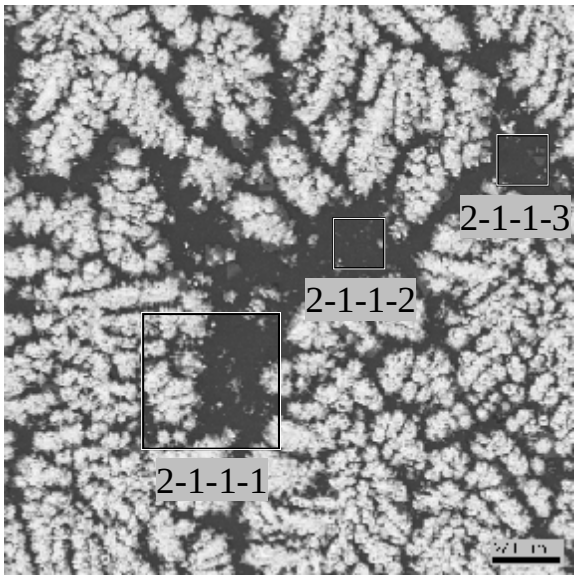

2-1-1

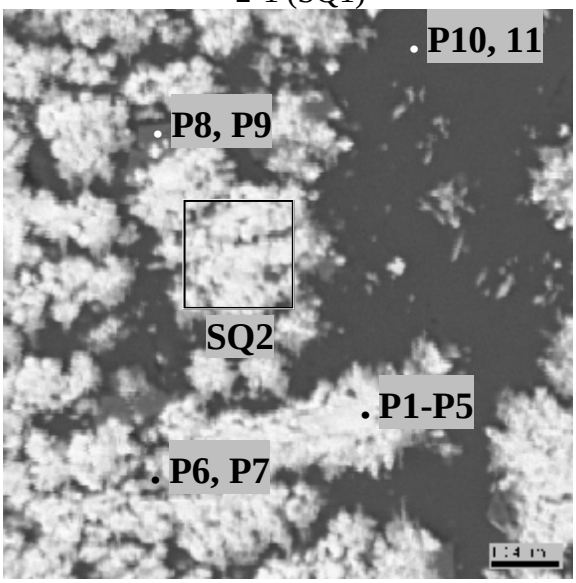

2-1-1-1

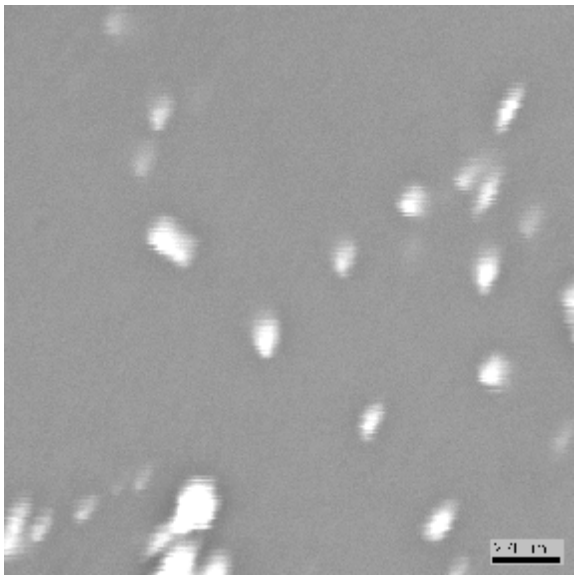

2-1-1-2 (SQ3)

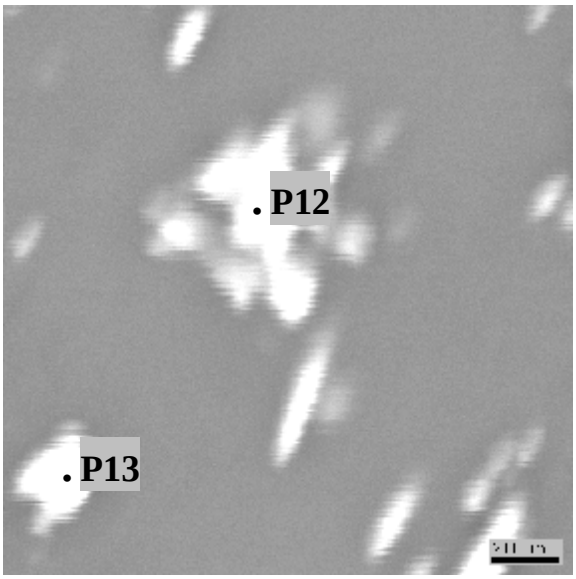

2-1-1-3 (SQ4)

Fig. 9. Micrographs of region 2

Table 9. EDX data for region 2

No.		UO_2	ZrO_2	SiO_2	CaO	$AlO_{1.5}$	FeO	$CrO_{1.5}$
SQ1	mass%	45.81	12.65	22.00	6.23	2.70	8.62	1.99
	mol.%	17.88	10.82	38.60	11.71	5.58	12.64	2.76
SQ2	mass%	60.66	15.67	10.21	3.09	1.60	5.14	3.61
	mol.%	30.88	17.48	23.36	7.57	4.33	9.84	6.53
SQ3	mass%	6.07	6.88	51.48	12.07	5.67	17.84	-
	mol.%	1.49	3.70	56.75	14.25	7.37	16.45	-
SQ4	mass%	7.28	7.49	50.39	12.03	5.29	17.28	0.24
	mol.%	1.81	4.08	56.35	14.41	6.97	16.16	0.22
P1	mass%	51.78	33.22	7.87	2.28	1.16	3.32	0.38
	mol.%	27.13	38.14	18.53	5.74	3.22	6.53	0.71
P2	mass%	64.25	16.42	10.67	2.95	1.42	4.28	-
	mol.%	34.54	19.35	25.79	7.63	4.06	8.64	-
P3	mass%	63.79	18.44	1.68	0.91	1.04	4.99	9.16
	mol.%	36.90	23.37	4.36	2.53	3.18	10.85	18.82
P4	mass%	81.66	14.46	1.46	0.95	-	1.10	0.37
	mol.%	62.84	24.38	5.05	3.54	-	3.17	1.02
P5	mass%	77.25	16.35	2.43	1.46	1.30	1.21	-
	mol.%	54.22	25.14	7.67	4.94	4.85	3.18	-
P6	mass%	77.16	17.31	2.17	1.26	0.70	1.40	-
	mol.%	55.16	27.11	6.97	4.35	2.63	3.77	-
P7	mass%	79.56	13.64	3.14	1.33	0.98	1.34	-
	mol.%	56.74	21.32	10.08	4.56	3.71	3.59	-
P8	mass%	1.31	1.67	2.81	0.48	6.42	30.48	56.82
	mol.%	0.35	0.99	3.41	0.63	9.18	30.93	54.51
P9	mass%	1.15	0.66	1.18	0.25	5.15	31.94	59.68
	mol.%	0.31	0.39	1.45	0.32	7.40	32.58	57.55
P10	mass%	3.01	4.35	55.27	12.87	5.82	18.68	-
	mol.%	0.71	2.25	58.59	14.62	7.27	16.56	-
P11	mass%	3.45	4.38	54.77	12.74	5.65	18.72	0.28
	mol.%	0.82	2.28	58.35	14.54	7.09	16.68	0.24
P12	mass%	29.63	11.85	34.22	8.19	4.02	12.08	-
	mol.%	9.39	8.23	48.74	12.50	6.75	14.39	-
P13	mass%	18.50	11.30	40.59	10.21	4.37	14.74	0.30
	mol.%	5.22	6.99	51.47	13.87	6.52	15.63	0.30

It can be seen that the dark-coloured phase (Fig. 9) is very rich in SiO_2, CaO and FeO (Tab. 9, SQ3, SQ4**,** points P10, P11). The light-coloured phase is rich in refractory components UO_2 and ZrO_2 (Tab. 9, SQ2, points P1-P5).

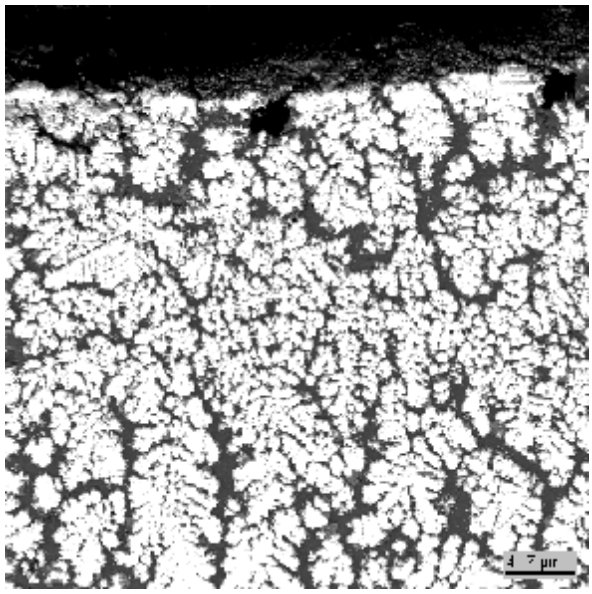

3 (SQ1)

Fig. 10. Micrograph of region 3

Table 10. EDX data for region 3

No.		UO_2	ZrO_2	SiO_2	CaO	$AlO_{1.5}$	FeO	$CrO_{1.5}$
SQ1	mass%	45.37	13.02	22.28	6.13	2.96	8.42	1.84
	mol.%	17.63	11.08	38.91	11.46	6.09	12.29	2.54

Regions 2 and 3 of the ingot from CORD46 represent microstructure of its upper part (Figs. 9 and 10). They have a similar character of crystallization and composition (Tabs. 9 and 10, SQ1).

Region 4 of the ingot (Fig. 11) represents its peripheral part closer to the bottom.

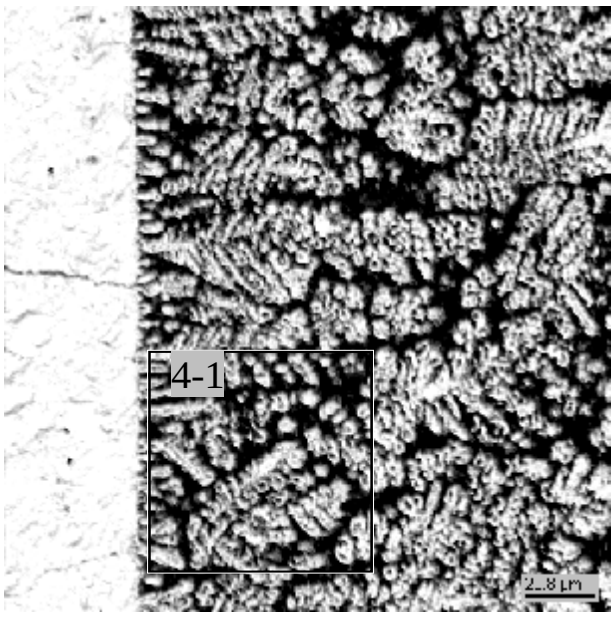

4

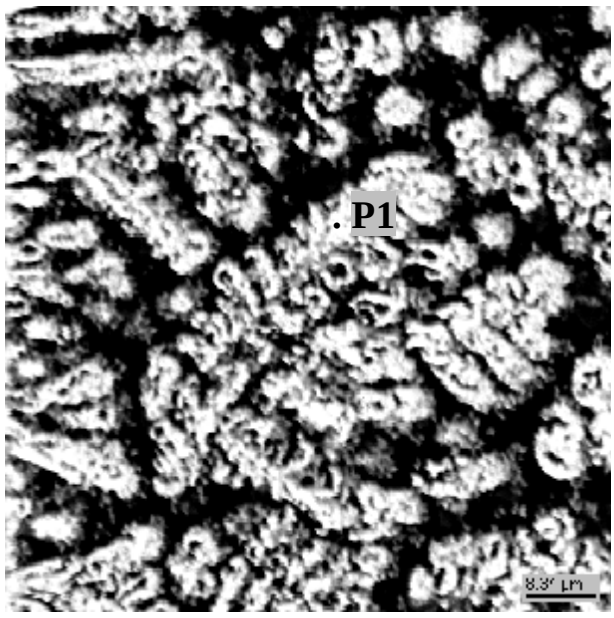

4-1

Fig. 11. Micrographs of region 4

Table 11. EDX data for region 4

No.		UO_2	ZrO_2	SiO_2	CaO	$AlO_{1.5}$	FeO	$CrO_{1.5}$
P1	mass%	89.29	9.99	-	0.72	-	-	-
	mol.%	77.89	19.10	-	3.02	-	-	-

Here, the light-coloured phase is also rich in refractory components (Tab. 11).

In general, the analysis of the crystallized melt microstructure has revealed uniform dendritic crystallization throughout the pool volume, except for the peripheral area. The analysis of the ingot lateral side (Fig. 8 and Tab. 8) showed the presence of a UO_2-based refractory phase layer.

Besides, it should be noted that the content of UO_2 was higher in melt samples than in the ingot, which may be explained by crystallization of this refractory phase on the cooled surfaces of the crucible at the HF heating switching off. The ingot bottom part has a layer that has not melted during the test and is clearly distinguishable in the macrosection. This is confirmed by measurements of the molten pool depth and bottom crust thickness.

3.4. Differential Thermal Analysis

Several crucible materials (e.g., Mo, W, etc.) were tested for their applicability in the differential thermal analysis (DTA) for T_{liq} determination. They were found to contaminate the melt, and thus hamper the analytical work.

Though T_{sol} measurement was not among the present work objectives, an attempt was made to determine it by DTA at lower temperatures. The SETSYS Evolution-2400 analyzer and the SETSOFT 2000 software package were used.

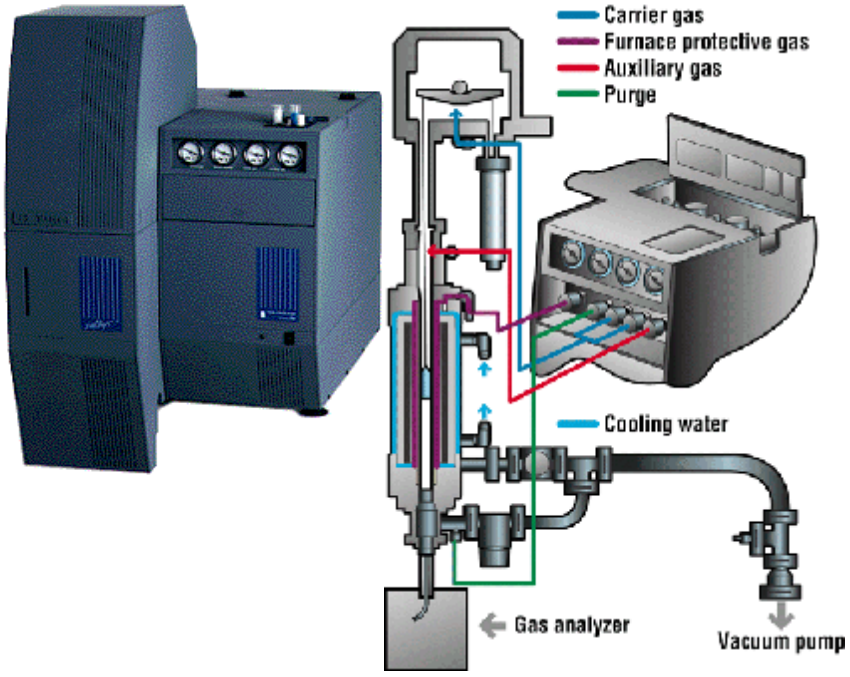

Fig. 12. SETSYS Evolution-2400, appearance and schematics

SETSYS Evolution-2400 (Fig.12) allows DSC, DTA, TG-DTA and TG-DSC measurements in a wide temperature range from 196° C up to 2400° C. The manufacturer-declared error of determining a phase transition temperature is ±2.5° C. The furnace working space may be either vacuumized, or filled with different gases/mixtures, e.g., air, argon, helium, carbon dioxide.

For the analysis, a ≈32 mg sample was prepared from the ingot central part. The crucible material was Pt. Before the analysis, the measurement cell was vacuumized and then filled with high-purity argon. The heating rate was 5° C/min, and a B-type thermocouple (Pt-30%Pt/Rh - 6% Rh) was used.

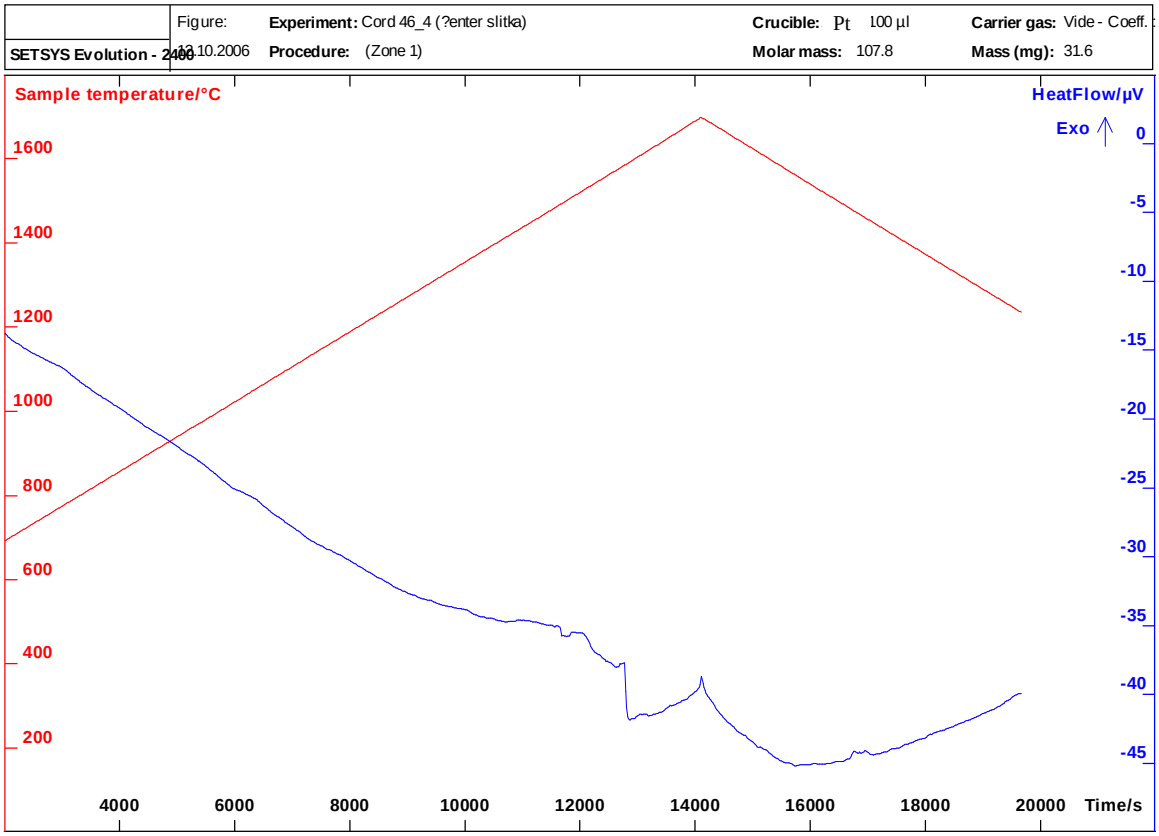

Fig. 13. DTA curve for an ingot sample from Cord46

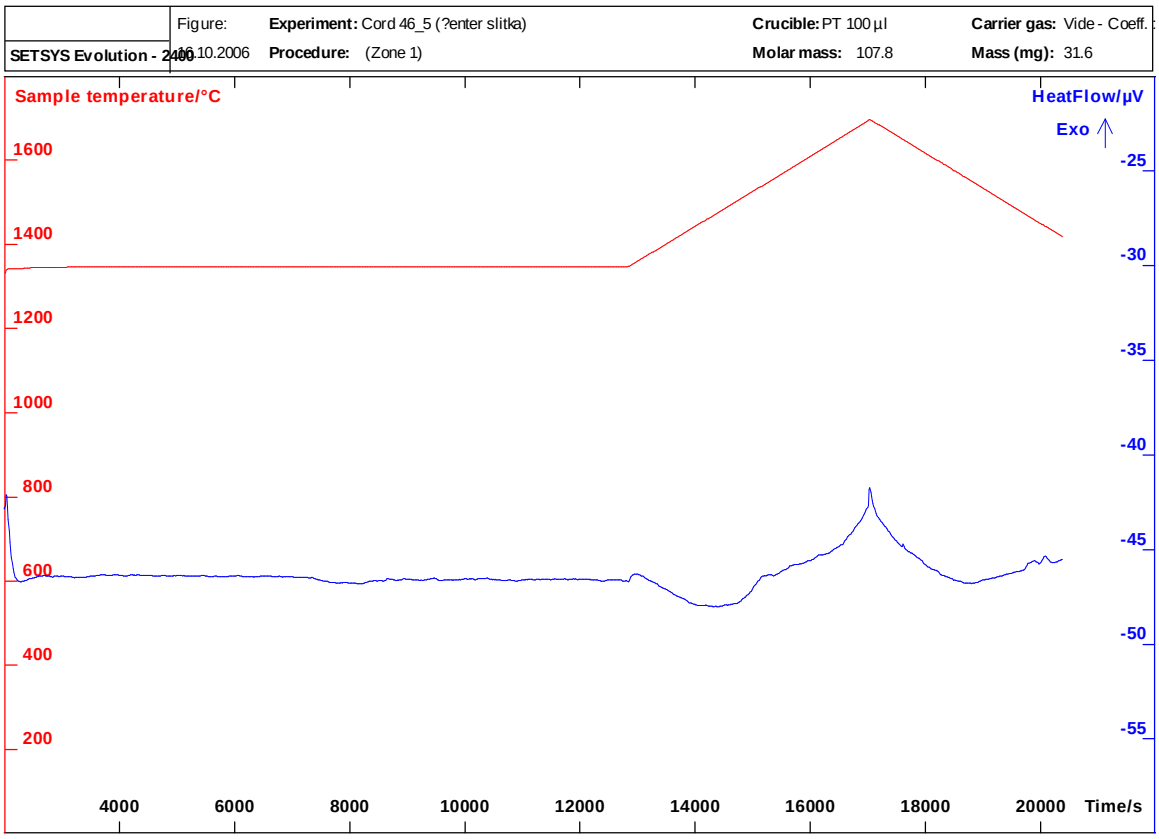

Fig. 14. DTA curve after sample annealing

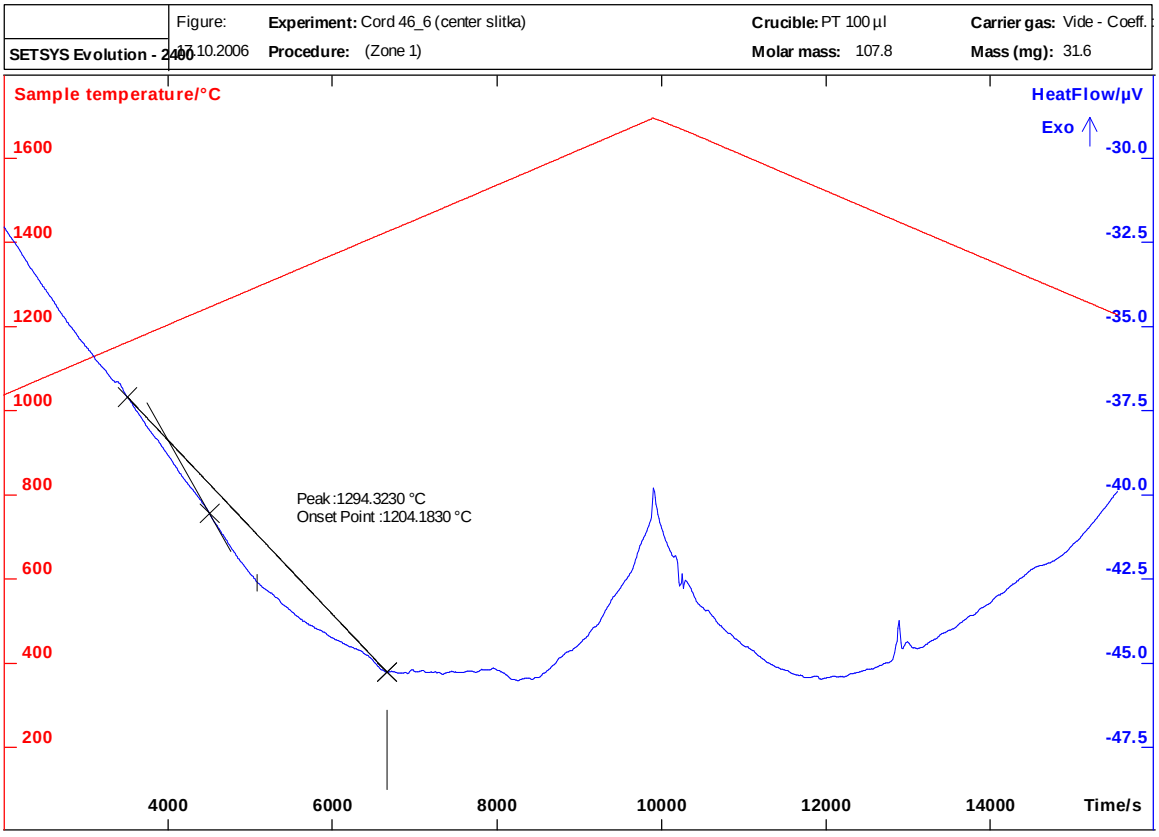

Fig. 15. DTA curve at lower temperatures after sample annealing

Fig. 13 shows a DTA curve the analysis of which has not revealed clearly expressed endothermic effects in the studied temperature domain. A possible reason of these effects absence may be the nonequilibrium, quenching-type crystallization of the multicomponent system. Phase transformations may happen during heating of such a sample, and it reflects in the DTA curve in the form of corresponding thermal effects.

For determining T_{sol} that would correspond to the equilibrium condition of the system, the same sample was annealed at 1350° C (Fig.14) and then subjected to DTA at a temperature above 1350° C. Then DTA temperature range was reduced. Fig. 15 shows a DTA curve with an indistinct endothermic effect that prevents precise determination of T_{sol}.

The absence of explicit thermal effects in the heating segment may be explained by the small quantity (Fig. 9, points 10, 11) of the first liquid, high viscosity and low thermal conductivity of the sample. The analysis of the implicit endothermic effect and the point of tangent line crossing with the baseline in the DTA curve show T_{sol} to be 1204° C. Other thermal effects could most likely be caused by polymorphous transformations (e.g., a tridymite to cristobalite, etc. transition is possible at 1480° C /3/).

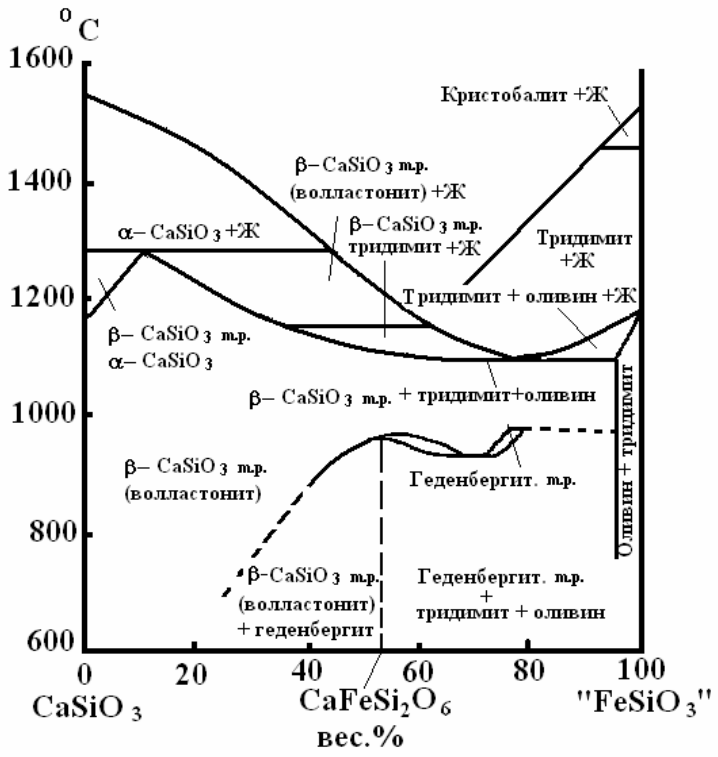

Fig. 16. Phase diagram of the $CaO \cdot SiO_2$–$FeO \cdot SiO_2$ specific system (according to Bowen et al. /3, 4/)

It should be noted that according to the SEM/EDX results the last-to-crystallize is the liquid rich in SiO_2, CaO, FeO (Tab. 9 points 10, 11). Data from the diagram of a specific system /3/ (Fig. 16) suppose that the temperature of such liquid solidification may be 1200-1300° C. Apparently, the presence of small quantities of other oxides in this liquid will not cause a significant change of T_{sol}.

4. Discussion of results

T_{liq} measurement in a prototypic multicomponent corium applying traditional methods involves severe technical difficulties because of the interaction of the melt with crucible materials. Application of VPA IMCC made it possible to perform the measurements.

In Sections 2 and 3.1 it has been mentioned that a considerable mass of solid crusts may lead to a changed melt composition in comparison with the loaded charge. In order to determine composition of the melt for which T_{liq} has been measured, it is possible to use findings for the melt samples taken during the measurements. The SEM/EDX results differ from those of XRF concerning the main components. This may be related to the nonuniform crystallization of the refractory phase at sampling, which is indirectly confirmed by and the SEM/EDX results for the ingot. Therefore, the XRF data were viewed as more reliable and hence used for determining the melt composition. It should be noted that the compositions determined from the XRF data for samples 2 and 3 (Tab. 4) are similar. The differences relate only to the aluminium oxide content. Taking into account that the SEM/EDX results confirmed the aluminium oxide concentration to be about 2 mass % in all samples (Tabs. 5-7), the XRF data for sample 3 were viewed as more reliable and used as resultant for determining the melt composition given in Tab. 12. The tabulated data show just an insignificant deviation from the specified composition.

Table. 12. Melt composition at T_{liq} measurement compared with the specified one

Composition	Content, mass%						
	UO_2	ZrO_2	FeO	SiO_2	CaO	Al_2O_3	Cr_2O_3
Specified composition	54.2	17.9	7.6	13.7	3.8	1.3	1.5
Melt composition as per sample 3	53.0	18.6	7.8	12.9	3.8	2.0	1.9

The performed research made it possible to determine composition and T_{liq} of a multicomponent system, as well as make an approximately estimate of T_{sol}. Tab. 13 offers a comparison between the measured T_{liq} and the results of thermodynamic calculations using the GEMINI-2 code and NUCLEA-06 database.

Table. 13. Experimentally obtained and calculated T_{liq} and T_{sol} values

Test	Composition, mass./at.%[1)–]								Experimental		Calculated	
	U	Zr	Fe	Si	Ca	Al	Cr	O	T_{liq}, ˚K	T_{sol}, ˚K	T_{liq}, ˚K	T_{sol}, ˚K
CORD	46.7	13.8	6.1	6.0	2.7	1.1	1.3	22.3	2493±30	≈1477	2290	1350
46	8.9	6.9	4.9	9.8	3.1	1.8	1.1	63.5				

5. Conclusions

The results of work performed in a new induction furnace designed for experiments with melts having low electric conductivity confirm that the VPA IMCC method is applicable for investigating ex-vessel multicomponent melts with a high silica content.

The measured T_{liq} differs from the calculated one for about 200 K. This discrepancy may give an impression about precision of modeling an multicomponent melt at the existing technical level.

The T_{sol} discrepancy may be due to the experimental error, small quantity of liquid at T_{sol}, low thermal conductivity and high viscosity of the SiO_2-containing melt.

References

1. Investigation of binary oxidic systems. System U-Zr-O. ISTC PROJECT # 1950.2. Final report, 2006Report on the U-Zr-O system.
2. Losev N.F. Quantitative X-ray fluorescence analysis. Moscow, Nauka Publishers. 1969. (Russ.)
3. Bowen N.L., Schairer J.F., Posnijak E., Am. J. Sci. 1933. V. 26. P. 193.
4. Toropov N.A., Barzakovsky V.P., Lapin V.V. et al. Phase diagrams of silicate systems. Reference book. Issue 3. Ternary silicate systems. Nauka Publishers, Leningrad Branch. 1972. P. 448. (Russ.)